

Multi-state current switching by voltage controlled coupling of crossed graphene nanoribbons

K. M. Masum Habib,^{1,a)} Ferdows Zahid,² and Roger K. Lake^{1,b)}

¹Department of Electrical Engineering, University of California, Riverside, California 92521-0204, USA

²Department of Physics, The University of Hong Kong, Hong Kong

(Received 1 August 2013; accepted 4 October 2013; published online 18 October 2013)

The interlayer transport between two semi-infinite crossed graphene nanoribbons (GNRs) is governed by the quantum interference between the standing waves of the individual GNRs. An external bias applied between the GNRs controls the wavelength and hence the relative phase of these standing waves. Sweeping the applied bias results in multiple constructive and destructive interference conditions. The oscillatory nature of the voltage controlled interference gives rise to an oscillatory current-voltage response with multiple negative differential resistance regions. The period of oscillation is inversely proportional to the length of the finite ends of the GNRs. Quantum interference is explicitly shown to be the physical mechanism controlling the interlayer current by direct evaluation of the interlayer matrix element using analytical expressions for the wavefunctions. © 2013 AIP Publishing LLC. [<http://dx.doi.org/10.1063/1.4826264>]

I. INTRODUCTION

One remarkable property of graphene is that the individual layers in misoriented or twisted bilayer graphene (TBG) are electronically decoupled.^{1–10} The decoupling results from the destructive quantum interference between the electron wave functions of the top and bottom graphene layers.⁵ Between two misoriented sheets of graphene, the coherent interlayer resistance has been found to vary between 8 and 16 orders of magnitude as the rotation angle is varied between 0° and 30°. ^{11,12} Contact resistances resulting from the coherent coupling between two rotated graphene layers have been calculated to vary between $\sim 10^7 \Omega \text{cm}^2$ and $\sim 10^{-9} \Omega \text{cm}^2$ as a function of the rotation angle.¹² The interlayer coupling is increased¹³ and the Fermi velocity is reduced¹⁴ in presence of a vertical electric field, and negative differential conductance is predicted at small biases.¹² Since the coherent interlayer coupling can be so small, the interlayer, room-temperature conductance for all but the smallest misorientation angles is dominated by phonon-assisted transport mediated by an out-of-plane beating mode of the bilayer with phonon energies ranging from 10 meV to 30 meV as the misorientation angle varies from 0° to 30°. ¹¹

The coherent electronic decoupling between two-dimensional (2D) misoriented bilayers is still present in lower dimensions, when the overlap region is reduced to the nanometer scale.¹⁵ The crystallographic misorientation angle of two overlapping armchair nanoribbons placed at a 90° angle with respect to each other is 30°. The coherent interlayer transmission between two crossed, 1.8 nm, armchair, graphene nanoribbons was suppressed by 5 orders of magnitude. Applying a 0.15 V, voltage between the nanoribbons increased the transmission by 4 orders of magnitude.¹⁵ The graphene nanoribbons (GNR) crossbar in Ref. 15 consisted

of two *infinite* nanoribbons in which the electron states were *propagating waves*.

This work investigates the electronic coupling between two *semi-infinite* armchair GNRs (aGNRs) in which the electron states are standing waves. Despite the equivalence of the atomistic geometry of the overlap regions, the inter-layer transport properties of the crossed infinite GNRs (IxGNR) and the crossed semi-infinite GNRs (SxGNR) differ due to the difference of the electronic wavefunctions. Unlike the current-voltage response of the IxGNR, sweeping a two-terminal voltage applied between the two crossed semi-infinite GNRs results in an oscillatory current-voltage (I–V) characteristic with multiple negative differential resistance (NDR) regions. Since the vibrational modes of such structures have not yet been calculated, only the coherent interlayer current will be considered. Estimates of the relative magnitudes of the coherent current and the phonon-assisted current will be given at the end.

The occurrence of transmission resonances and antiresonances in single layer graphene structures is not uncommon.^{16–23} Such structures would display many features in the *low-bias conductance* as a function of gate voltage. In contrast, the individual features in the transmission spectra of the rotated graphene nanoribbons are not of primary importance. The *average magnitude* of the transmission and the dependence of the average magnitude on the applied *two terminal* voltages are of primary interest. Sweeping an external two-terminal bias applied between the GNRs alters the relative phases of the two standing waves resulting in a periodic modulation of the *average* interlayer transmission and an oscillatory I–V characteristic with multiple NDR regions. The voltage period of oscillation is inversely proportional to the length of the truncated ends of the GNRs.

A GNR device with oscillatory I–V characteristics and multiple NDR regions is complementary to numerous graphene field effect transistors.^{24–29} Such a non-linear I–V

^{a)}Email: khabib@ee.ucr.edu

^{b)}Email: rlake@ee.ucr.edu

response can provide increased functional density in all-carbon based electronics.^{30–32}

II. METHOD

Three different types of calculations are performed. (i) The geometry of the graphene nanoribbons are optimized using density functional theory (DFT). (ii) The electronic transport is calculated using the non-equilibrium Green's function (NEGF) formalism. The Hamiltonian matrix elements used in the NEGF calculations are generated using the extended Hückel theory (EHT). (iii) The physics governing the electron transport is explained by direct evaluation of the interlayer matrix element using analytical expressions for the wavefunctions.

A. Device structure and transport

The structure, as shown in Fig. 1, consists of two overlapping, semi-infinite, armchair GNRs. The GNRs are H-passivated, and their structure is relaxed using a projector augmented wave method within the framework of the Perdew-Burke-Ernzerhof type generalized gradient approximation of the density functional theory as implemented in the software package VASP.³³ The relaxed GNRs are placed one above the other to create the crossbar, and no further relaxation is performed. The vertical separation between the GNRs is taken to be 3.35 Å, which is the separation between the graphene layers observed in graphite.³⁴ Recent atomic force microscopy measurements of crossed single layer graphene used statistical fitting to determine an interlayer distance of $d \approx 4$ Å.¹⁰

Each GNR has one truncated end with a zigzag edge. To minimize the bandgap resulting from the finite width, the number of atoms across the width of the GNRs is chosen to

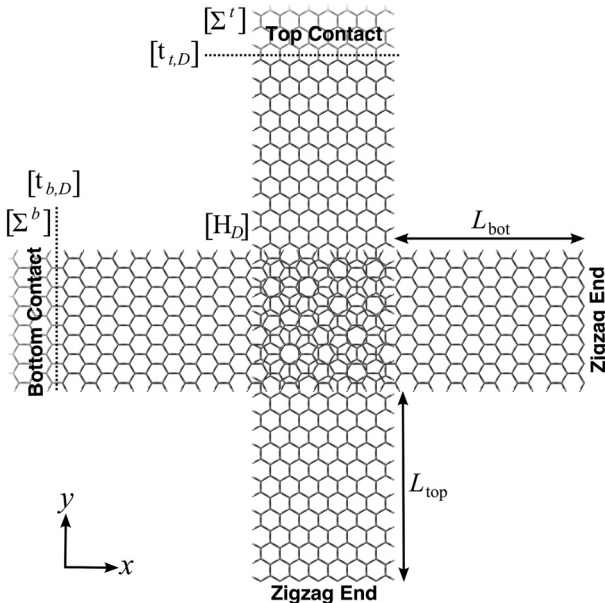


FIG. 1. The structure consists of two crossed semi-infinite, armchair nanoribbons. To minimize the bandgap due to quantization, the number of atoms across the width is chosen to be $3p + 2$, where p is an integer. The length of the top and bottom truncated ends are L_{top} and L_{bot} , respectively. The coordinate system is chosen such that the origin is at the center of the overlap region.

be $N_w = 3p + 2$, where p is an integer. The analysis is carried out for $N_w = 14$ with a calculated bandgap of 136 meV. The bandgap is a consequence of the reduced C-C bond lengths at the armchair edges of the relaxed GNR.^{35,36} Different and unequal widths are also numerically simulated.

The top and bottom contacts are modeled as infinite leads using self-energies Σ^t and Σ^b on the top GNR (tGNR) and the bottom GNR (bGNR), respectively, as shown in Fig. 1. An external bias V is applied between the tGNR and the bGNR such that the electrostatic potential energies are $U(\mathbf{r}) = -eV/2$ for atoms on the tGNR and, $U(\mathbf{r}) = eV/2$ for atoms on the bGNR. The Hamiltonian matrix elements used in the NEGF calculation are generated from the EHT using non-orthogonal Slater-type orbitals. The EHT graphene parameters are taken from Ref. 37. The Hamiltonian matrix elements are used in the NEGF algorithm to calculate the transmission coefficient, $T(E)$, as described in Ref. 15. The current is calculated from

$$I = \frac{2e}{\hbar} \int \frac{dE}{2\pi} T(E) [f_b(E) - f_t(E)], \quad (1)$$

where $f_b(E)$ and $f_t(E)$ are the Fermi distributions of the bGNR and tGNR contacts, respectively. In all current calculations, the temperature of the Fermi distributions is 300 K.

B. Analytical model

The analytical expression for the inter-layer transmission obtained using Fermi's Golden Rule is given by¹⁵

$$T(E) = 4\pi^2 \sum_{m,n} |M_{m,n}|^2 N_n(E - eV/2) N_m(E + eV/2), \quad (2)$$

where the subscripts m and n index a mode on the top and bottom GNR, respectively, $N_m(E)$ and $N_n(E)$ are the corresponding single-spin density of states, and $M_{m,n} = \langle \psi_{mk_y} | H_{int} | \psi_{nk_x} \rangle$ is the matrix element between the states on the top and bottom GNRs. Here, $|\psi_{mk_y}\rangle$ is the injected state at the top contact, and $|\psi_{nk_x}\rangle$ is the collected state at the bottom contact. Both states are at energy E . Since the low energy transport of the SxGNR is governed by the fundamental modes, we will only consider the wavefunctions of the conduction and valance bands and drop the subscripts of M below.

Within the framework of the continuum model, the wavefunction of mode n of the semi-infinite aGNR shown in Fig. 2 can be written as^{38,39}

$$|\psi_{nk_y}\rangle = |\psi_{nk_y,A}\rangle + |\psi_{nk_y,B}\rangle \quad (3)$$

with

$$|\psi_{nk_y,\alpha}\rangle = \sum_{\mathbf{R}_\alpha} (e^{i\mathbf{K}\cdot\mathbf{R}_\alpha} \psi_{n\alpha} - e^{i\mathbf{K}'\cdot\mathbf{R}_\alpha} \psi'_{n\alpha}) |\alpha_{\mathbf{R}_\alpha}\rangle, \quad (4)$$

where $|\alpha_{\mathbf{R}_\alpha}\rangle$ is the p_z orbital of the carbon atom located at \mathbf{R}_α with $\alpha \in \{A, B\}$, $\psi_{n\alpha}$ and $\psi'_{n\alpha}$ are envelope wave functions at $K \equiv (-4\pi/3a_0, 0)$ and $K' \equiv (4\pi/3a_0, 0)$ valleys, respectively. The envelope wave functions of π -electrons can be written as a four components spinor^{38,39}

$$\begin{bmatrix} \psi_{nA} \\ \psi_{nB} \\ -\psi'_{nA} \\ -\psi'_{nB} \end{bmatrix} = C_1 \begin{bmatrix} \sin(k_y y_A) e^{i k_{nx} x_A} \\ \frac{s}{k_n} \left(-k_{nx} \sin(k_y y_B) e^{i k_{nx} x_B} + k_y \cos(k_y y_B) e^{i k_{nx} x_B} \right) \\ -\sin(k_y y_A) e^{-i k_{nx} x_A} \\ \frac{s}{k_n} \left(k_{nx} \sin(k_y y_B) e^{-i k_{nx} x_B} - k_y \cos(k_y y_B) e^{-i k_{nx} x_B} \right) \end{bmatrix} \quad (5)$$

with

$$k_n = \sqrt{k_{nx}^2 + k_y^2}, \quad (6)$$

where $s = +1$ and -1 for the conduction and valance bands, respectively. The quantized wavevector k_{nx} is given by

$$k_{nx} = \tilde{k}_{nx} - \frac{2\pi}{3a_0}, \quad (7)$$

where $n = 0, \pm 1, \pm 2, \dots$ and $\tilde{k}_{nx} = \frac{2n\pi}{(N_w+1)a_0}$. The dispersion relationship of the electron associated with the wavefunction in Eq. (3) is

$$E_n(k_y) = s\gamma k_n = s\hbar v k_n, \quad (8)$$

where $\gamma = \frac{\sqrt{3}a_0 t_0}{2} = \hbar v$, $t_0 = 2.7$ eV is the nearest neighbor tight binding parameter⁴⁰ and v is the velocity of electron near the Dirac point of graphene. One difference between the wavefunction of a semi-infinite aGNR given by Eq. (5) and the wavefunction of a graphene quantum dot (GQD) derived in Ref. 38 is that in a GQD, k_y is discrete due to the fourth hard-wall boundary imposed on the GQD.

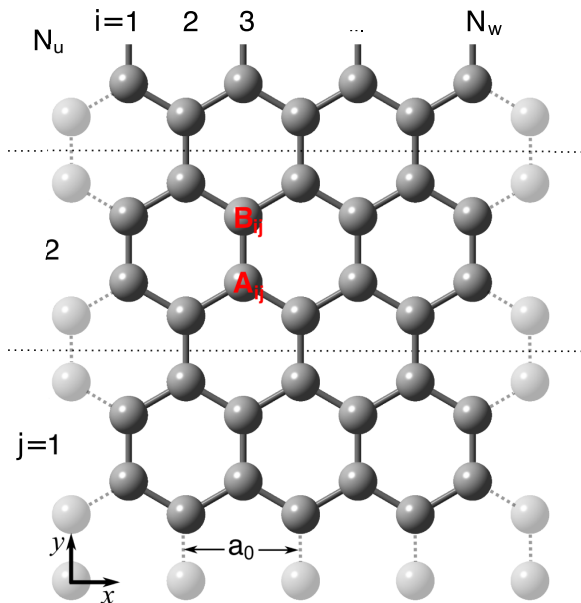


FIG. 2. Atomistic geometry of the model semi-infinite aGNR with a zigzag end. The origin of the coordinate system is placed on the atom at the bottom left corner. The edge-atoms removed from the GNR are shown in gray. The envelope function is zero at those positions. For the analytical calculations presented in Sec. IV, the GNR width $N_w = 14$.

For a $N_w = 3p + 2$ atomic layer wide metallic aGNRs, the band index for the conduction and valance band is given by $n = p + 1$. Hence, $k_{nx} = 0$ and the dispersion relationship for these bands is linear

$$E_n(k_y) = s\gamma k_y = s\hbar v k_y. \quad (9)$$

The corresponding wavefunction components obtained from Eqs. (4)–(6) are given by

$$|\psi_{nk_y, \alpha}\rangle = C \sum_i^{N_w} \sum_j^{N_u} \phi_{k_y, \alpha}(j) \sin(\tilde{k}_{nx} x_{\alpha i}) |\alpha_{ij}\rangle, \quad (10)$$

where the envelope wavefunctions along y

$$\phi_{k_y, A}(j) = \sin(k_y y_{A_j}) \quad (11)$$

and

$$\phi_{k_y, B}(j) = s \cos(k_y y_{B_j}) \quad (12)$$

are standing waves. Here, the normalization constant $C = \sqrt{\frac{2}{(N_w+1)N_u}}$, $\tilde{k}_{nx} = \frac{2\pi}{3a_0}$ and $|\alpha_{ij}\rangle$ is the p_z orbital of the atomic site α in the atomic layer i and the unit cell j of the aGNR.

This continuum model does not take into account the reduced C-C bond length at the armchair edges and therefore $N_w = 3p + 2$ atomic layer wide aGNRs do not show any bandgap. Also, this model does not include the edge state localized at the zigzag edge of the truncated end. Although it does not include the bandgap and the edge states, in Sec. IV, we will show that this model captures the essential physics governing the quantum transport in the SxGNR. The missing transmission features corresponding to the bandgap and the edge states do not affect the conclusions drawn by this continuum description.

The coordinate system of the SxGNR shown in Fig. 1 is chosen such that the origin is located at the center of the overlap region. The top and bottom stubs are equal in length, i.e., $L_{bot} = L_{top} \equiv L$. In this coordinate system, the envelope wavefunctions along y for the fundamental modes of the tGNR are

$$\phi_{k_y, A}(j) = \sin k_y (y_{A_j} + L_s) \quad (13)$$

and

$$\phi_{k_y, B}(j) = s \cos k_y (y_{B_j} + L_s), \quad (14)$$

where the stub length L_s is measured from the origin, i.e., $L_s = L + W/2$. Here, W is the width of the GNRs. Similarly,

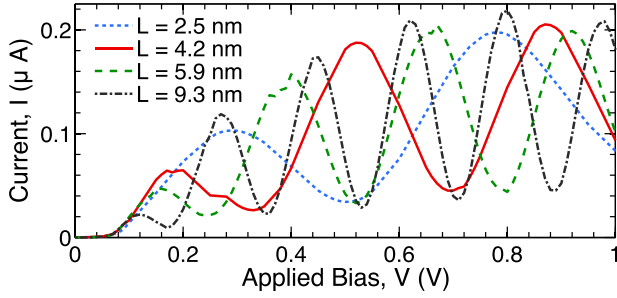


FIG. 3. Current voltage characteristics of a symmetric SxGNR with different stub-lengths as shown in the legend.

the envelope wavefunctions for the fundamental modes of the bGNR are obtained by replacing y with $-x$ in Eqs. (13) and (14)

$$\phi_{k_x A}(j) = -\sin k_x(x_{A_j} - L_s), \quad (15)$$

$$\phi_{k_x B}(j) = s \cos k_x(x_{B_j} - L_s). \quad (16)$$

For the fundamental modes, the quantized wavevectors for the tGNR and the bGNR are equal, i.e., $q_n \equiv \tilde{k}_{nx} = \tilde{k}_{ny}$.

The matrix element M between a k_y state of the tGNR and a k_x state of the bGNR can be resolved into four components

$$M = M_{AA} + M_{AB} + M_{BA} + M_{BB}, \quad (17)$$

where the subscripts indicate the A or B atom of each primitive unit cell. The matrix elements are given by

$$M_{\alpha\beta} \equiv \langle \psi_{k_y\alpha} | H_{int} | \psi_{k_x\beta} \rangle, \quad (18)$$

$$= C^2 \sum_{i,j,i',j'} \phi_{k_y\alpha}(j) \phi_{k_x\beta}(j') \sin(q_n x_{\alpha i}) \sin(q_n y_{\beta j'}) t_{ij,i'j'}, \quad (19)$$

where i, j , and i', j' are the indices of the atoms on the top and the bottom GNRs, respectively. The inter-layer matrix elements between the π -orbitals are obtained following Ref. 13 with $t_{ij,i'j'} = -t_1 e^{-3(d_{ij,i'j'} - d_o)}$, where $d_{ij,i'j'}$ is the distance between the atom on the top layer at site (i, j) and the atom on the bottom layer at site (i', j') , and d_o is the distance between the two layers (3.35 Å). The inter-layer parameter $t_1 = 0.36$ eV.⁴⁰

Since the site energies of the top and bottom GNRs are shifted by $+eV/2$, and $-eV/2$, respectively, the wavevectors for the top and bottom GNRs are given by

$$k_y = \frac{1}{s\gamma} \left(E + \frac{eV}{2} \right) \quad (20)$$

and

$$k_x = \frac{1}{s\gamma} \left(E - \frac{eV}{2} \right), \quad (21)$$

respectively. Hence, the external bias can be used to control the relative phase of the envelope wavefunctions inside the overlap region. In Sec. IV, we show that this voltage

controlled phase determines the nature of the interference between the standing waves of the tGNR and bGNR.

III. NUMERICAL RESULTS

The inter layer current in the SxGNR, calculated using the NEGF and EHT formalism, is an oscillatory function of the applied bias with multiple NDR regions as shown in Fig. 3. The period of oscillations are 0.5 V, 0.35 V, 0.27 V, and 0.18 V for SxGNRs with stub lengths 2.5 nm, 4.2 nm, 5.9 nm, and 9.3 nm, respectively. Using an analytical model, we show below that the period of oscillation is inversely proportional to the stub length.

The inter-GNR transmission plots for stub length $L = 4.2$ nm at the current minima and maxima are shown in Fig. 4. At zero bias, the transmission shown in Fig. 4(a) is strongly suppressed within -0.25 eV $< E < 0.5$ eV due to the destructive interference between the standing waves of the top and bottom GNR states as explained in Sec. IV below. The dip in the transmission near $E = 0$ eV is due to the 136 meV bandgap of the top and bottom GNRs. The narrow peak in the transmission at $E = 0$ eV results from the edge states localized at the zigzag edges of the top and the bottom GNRs.⁴¹

When the bias is increased to 0.2 V, the transmission increases by five orders of magnitude as shown in Fig. 4(b) and the current reaches its first maximum. The transmission peaks at $E = -0.1$ eV and $E = 0.1$ eV are due to the edge states of the top and the bottom GNR, respectively. This is confirmed by the three dimensional contours of the local density of states shown in Fig. 5. The states at $E = -0.1$ eV and $E = 0.1$ eV are localized at the zigzag edges of the top and the bottom GNR, respectively.

To understand the contribution of the edge states to the total current, we have plotted the cumulative current in Fig. 4. The expression of cumulative current is $I_{cum}(E) = \frac{2e}{h} \int_{-\infty}^E \frac{dE'}{2\pi} T(E') [f_b(E') - f_t(E')]$, where f_b and f_t are the Fermi distributions at the bottom and the top contacts, respectively. At $V = 0.2$ V, the majority of the current is transferred through the evanescent edge states at $E = \pm 0.1$ eV as indicated by I_{cum} in Fig. 4(b). However, at $V = 0.52$ V and $V = 0.88$ V all of the states within the Fermi window contribute to the current as shown in Figs. 4(d) and 4(f), respectively.

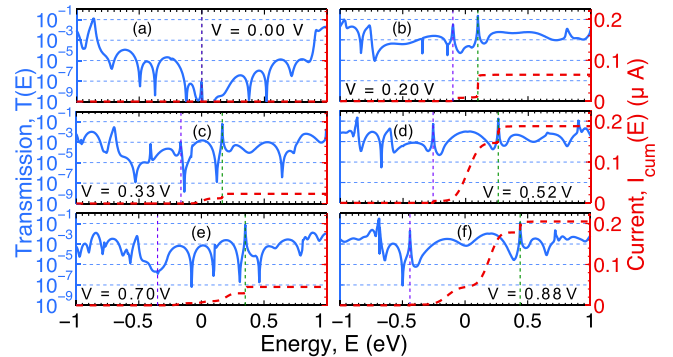


FIG. 4. Transmission (solid line) and the cumulative current (dashed line) as functions of energy for $L = 4.2$ nm at the current minima and maxima. The vertical lines represent chemical potentials of the top and the bottom contacts.

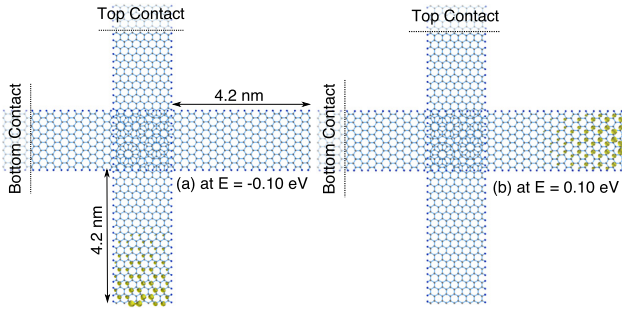


FIG. 5. Three dimensional contour plots of local density of states (LDOS) for $V = 0.2$ V and $L = 4.2$ nm at (a) $E = -0.1$ eV and (b) $E = 0.1$ eV.

It is found that up to the first current minimum, the I–V is governed by the interference between the edge state and the standing wave. Since the edge state decays exponentially inside the GNR, the matrix element between the edge state of one GNR and the standing wave of the other GNR decreases with increasing stub length. This explains the lowering of the first peak in the I–V with increasing stub length.

At $V = 0.33$ V and 0.7 V, the transmission decreases due to the destructive interference between the standing waves of the tGNR and the bGNR and the current minima appear in the I–V. In Sec. IV, we will show that with increasing bias the successive appearance of the constructive and destructive interference leads to successive enhancement and suppression of the interlayer transmission, and hence the current oscillates.

To determine if the current-voltage response was qualitatively the same for variations of the symmetric geometry shown in Fig. 1, we carried out a preliminary study of three asymmetric structures: (a) $L_{bot} = 2.5$ nm, $L_{top} = 4.2$ nm, $N_w = 14$, (b) $L_{bot} = \infty$, $L_{top} = 4.2$ nm, $N_w = 14$, and (c) $N_w = 20$ (14) for the top (bottom) GNR with $L_{top} = L_{bot} = 4.2$ nm. The current-voltage responses remain similar to those shown in Fig. 3. The periods of oscillation for the (a), (b), and (c) configurations are 0.4 V, 0.44 V, and 0.36 V, respectively. For the (b) configuration with one infinite GNR, the first current peak becomes smaller due to absence of one of the edge states.

To determine how a built-in potential difference between the top and bottom GNRs affects the current-voltage response, we simulated the same four structures as in Fig. 3 with a built-in potential difference of 0.25 V. A forward bias drives the potential difference between the two GNRs to

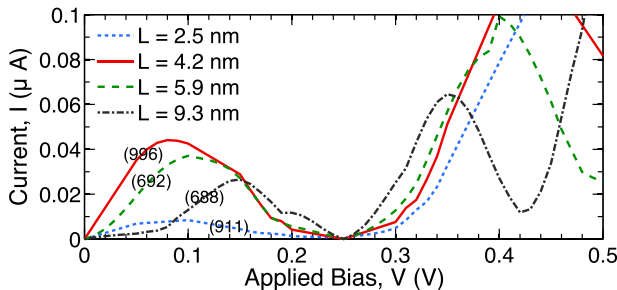


FIG. 6. Simulated I–V characteristics of SxGNR p–n junctions with built-in potential, $\phi_{bi} = 0.25$ V for different stub lengths. The numbers inside the parentheses represent the peak-to-valley current ratios.

zero. When the potential difference is zero, the transmission is reduced several orders of magnitude as shown in Fig. 4(a). At this bias (0.25 V), the current is reduced by several orders of magnitude. The current-voltage curves of the 4 structures with a built-in voltage of 0.25 V are shown in Fig. 6. The current ratio of the first current peak to the current minimum at 0.25 V is given in parenthesis for each curve. Because of the large reduction in transmission, when the GNRs are drive to equal potentials, peak-to-valley ratios of approximately three orders of magnitude are observed.

IV. ANALYSIS

Analysis based on Fermi's Golden Rule and analytical expressions for the wavefunctions reveals the physics of the inter-GNR transport. The transmission is governed by both the matrix element squared and the density of states as shown in Eq. (2). The transmission calculated numerically with NEGF and the matrix element squared calculated from the analytical expressions for the wavefunctions are plotted in Figs. 7(a) and 7(b). A comparison of the plots shows that the energy dependence of the transmission and the overall change in magnitude with bias are determined by the matrix element. The mismatch between $T(E)$ and $|M(E)|^2$ near $E = 0$ eV in Fig. 7(a) is due to the fact that the bandgap and the edge state are not included in the analytical model. Outside of that 136 meV range, the energy dependence of $T(E)$ follows closely that of $|M(E)|^2$. Similarly, the matrix element squared at $V = 0.2$ V shown in Fig. 7(b) captures the enhancement of the transmission at low energies by the applied bias. The peaks in the $T(E)$ plot at $E = \pm V/2$ are due to the edge states and are not reproduced in the $|M(E)|^2$ plot. Overall, the matrix element governs the voltage dependence of the transmission, and we shall concentrate only on M below.

The four components of the matrix element given by Eqs. (17) and (19) are plotted in Figs. 7(c) and 7(d). The total matrix element, M , is well approximated by the sum of M_{AB} and M_{BA} , since these two matrix elements are orders of magnitude larger than either M_{AA} or M_{BB} . At $V = 0$ V, M_{AB} and M_{BA} are approximately equal in magnitude but 180° out of phase as shown in Fig. 7(c). Thus, the destructive interference between the AB and the BA components of M suppresses the total matrix element and hence the transmission.

When the bias is increased to 0.2 V, the quantum phases of the standing electron waves are modulated by the bias and M_{AB} and M_{BA} acquire a non-zero average value as shown in Fig. 7(d). As a result, the AB and BA components do not cancel.

The nature of the voltage controlled quantum interference can be understood by looking at the envelope wavefunctions in the long wavelength limit. At low energies, when the wavelength $\lambda \gg W$, the variation of the envelope function inside the overlap region is negligible, i.e., $\phi_{k_y,A}(j) = \sin k_y(y_{A_j} + L_s) \approx \sin(k_y L_s)$. Using the dispersion relationship given by Eq. (20), we get

$$\phi_{k_y,A}(j) \approx \sin \frac{L_s}{\gamma} (E + eV/2). \quad (22)$$

Similarly, for the B sites of bGNR

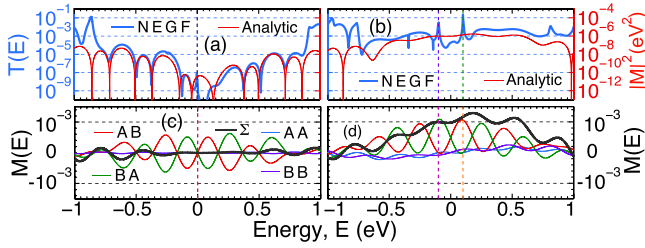


FIG. 7. Transmission $T(E)$ (thick line) and matrix element $|M(E)|^2$ (thin line) at (a) $V=0$ V and (b) $V=0.2$ V. Four components of matrix element $M = M_{AA} + M_{AB} + M_{BA} + M_{BB}$ labeled as AA, AB, BA, and BB at (c) $V=0$ V and (d) $V=0.2$ V. The black thick line shows the sum of the four matrix elements, M .

$$\phi_{k,\beta}(j) \approx s \cos \frac{L_s}{\gamma} (E - eV/2). \quad (23)$$

Using Eqs. (19), (22), and (23), we get the expression for M_{AB} in the long wavelength limit

$$M_{AB} \approx \frac{1}{2} \left(\sin \frac{2L_s E}{\gamma} + \sin \frac{L_s eV}{\gamma} \right) H_{AB}. \quad (24)$$

Similarly,

$$M_{BA} \approx \frac{1}{2} \left(\sin \frac{2L_s E}{\gamma} - \sin \frac{L_s eV}{\gamma} \right) H_{BA}. \quad (25)$$

Here, the quantity $H_{\alpha\beta}$ is the energy independent part of $M_{\alpha\beta}$ that depends on the atomic positions of the α atoms of the tGNR and the β atoms of the bGNR

$$H_{\alpha\beta} = C^2 \sum_{i,j,i',j'} \sin(q_n x_{\alpha i}) \sin(q_n y_{\beta j'}) t_{ij i' j'}. \quad (26)$$

Numerical calculations show that

$$H_{BA} = -H_{AB}. \quad (27)$$

The quantity, H_{AB} (H_{BA}) is the weighted sum of the inter-layer hopping parameter between all the A (B) atoms of the tGNR and all the B (A) atoms of the bGNR weighted by the transverse sine functions of $|\psi_{n k_x, A(B)}\rangle$ and $|\psi_{n k_y, B(A)}\rangle$. Thus, they are sums over different matrix elements and are not Hermitian conjugates.

Using relation (27) in Eqs. (24) and (25), we get the final expressions for M_{AB} and M_{BA}

$$M_{AB} \approx \frac{1}{2} \left(\sin \frac{2L_s E}{\gamma} + \sin \frac{L_s eV}{\gamma} \right) H_{AB}, \quad (28)$$

$$M_{BA} \approx \frac{1}{2} \left(-\sin \frac{2L_s E}{\gamma} + \sin \frac{L_s eV}{\gamma} \right) H_{AB}. \quad (29)$$

Eqs. (28) and (29) clearly show that at $V = n \frac{\pi\gamma}{eL_s}$, where $n = 0, 1, 2, \dots$, the AB and the BA components of the matrix element cancel each other as indicated in Fig. 7(c). Thus, the voltage controlled destructive interference between the A and the B atoms results in suppression of transmission and current minima. Similarly, at $V = (2m+1) \frac{\pi\gamma}{2eL_s}$, where $m = 0, 1, 2, \dots$, the A and B atoms interfere constructively giving rise to enhancement in transmission and current

maxima. Thus, the voltage controlled interference between the tGNR and the bGNR is an oscillatory function of the bias, which results in an oscillatory current voltage response with multiple NDR regions. The period of the oscillation is inversely proportional to the stub length

$$V_p = \frac{\pi\gamma}{eL_s}. \quad (30)$$

The periods of the oscillations in the current-voltage responses calculated using Eq. (30) are 0.52 V, 0.35 V, 0.26 V, and 0.18 V for the SxGNRs with 2.5 nm, 4.2 nm, 5.9 nm, and 9.3 nm stub lengths, respectively, which closely match with the numerical results calculated using NEGF.

With an understanding of the magnitude of the coherent current, we can compare it to an estimate of the magnitude of the phonon assisted current. Since the phonon modes of the structures under consideration are not known, we estimate an order-of-magnitude of the phonon-assisted current from the phonon-assisted conductivity G_{ph} of 2D misoriented graphene. In 2D misoriented graphene, G_{ph} is a smoothly decreasing function of the rotation angle. At low temperature ($T = 20$ K) and finite bias, $V > 0.1$ V, the inter-layer conductance lies between 10^{-9} S/nm² and 10^{-8} S/nm².¹¹ The overlap region of the crossbar in Fig. 3 is 3.24 nm². Choosing a 1 V bias, the maximum estimate of the phonon-assisted current would be 32.4 nA. The coherent current shown in Fig. 3 is on the order of 100 nA. Thus, from this crude estimate, the current oscillations in the coherent current should still be observable in the presence of phonon-assisted current.

V. CONCLUSIONS

The inter-layer transport between two crossed, semi-infinite armchair GNRs is governed by voltage controlled quantum interference between the standing waves of the individual GNRs. An external bias applied between the GNRs controls the wavelength and hence the relative phases of these standing waves. Sweeping the applied two-terminal bias causes multiple constructive and destructive interference conditions resulting in a periodic modulation of the average transmission and an oscillatory I-V characteristic with multiple NDR regions. The voltage period of the oscillation is inversely proportional to the length of the truncated ends of the GNRs. An estimate of the magnitude of the phonon-assisted current based on the 2D phonon-assisted conductivity indicates that the oscillations in the coherent current will not be masked by the phonon-assisted current.

ACKNOWLEDGMENTS

This work was supported in part by FAME, one of the six centers of STARnet, a Semiconductor Research Corporation program sponsored by MARCO and DARPA.

¹J. M. B. Lopes dos Santos, N. M. R. Peres, and A. H. Castro Neto, *Phys. Rev. Lett.* **99**, 256802 (2007).

²X. Wu, X. Li, Z. Song, C. Berger, and W. A. de Heer, *Phys. Rev. Lett.* **98**, 136801 (2007).

- ³S. Latil, V. Meunier, and L. Henrard, *Phys. Rev. B* **76**, 201402 (2007).
- ⁴J. Hass, F. Varchon, J. Millán-Otoya, M. Sprinkle, N. Sharma, W. de Heer, C. Berger, P. First, L. Magaud, and E. Conrad, *Phys. Rev. Lett.* **100**, 125504 (2008).
- ⁵S. Shallcross, S. Sharma, and O. A. Pankratov, *Phys. Rev. Lett.* **101**, 056803 (2008).
- ⁶S. Shallcross, S. Sharma, E. Kandelaki, and O. A. Pankratov, *Phys. Rev. B* **81**, 165105 (2010).
- ⁷G. Trambly de Laissardiere, D. Mayou, and L. Magaud, *Nano Lett.* **10**, 804 (2010).
- ⁸A. Luican, G. Li, A. Reina, J. Kong, R. R. Nair, K. S. Novoselov, A. K. Geim, and E. Y. Andrei, *Phys. Rev. Lett.* **106**, 126802 (2011).
- ⁹J. M. B. Lopes dos Santos, N. M. R. Peres, and A. H. Castro Neto, *Phys. Rev. B* **86**, 155449 (2012).
- ¹⁰Y. Kim, H. Yun, S.-G. Nam, M. Son, D. S. Lee, D. C. Kim, S. Seo, H. C. Choi, H.-J. Lee, S. W. Lee, and J. S. Kim, *Phys. Rev. Lett.* **110**, 096602 (2013).
- ¹¹V. Perebeinos, J. Tersoff, and P. Avouris, *Phys. Rev. Lett.* **109**, 236604 (2012).
- ¹²R. Bistritzer and A. H. MacDonald, *Phys. Rev. B* **81**, 245412 (2010).
- ¹³E. S. Morell, P. Vargas, L. Chico, and L. Brey, *Phys. Rev. B* **84**, 195421 (2011).
- ¹⁴L. Xian, S. Barraza-Lopez, and M. Chou, *Phys. Rev. B* **84**, 075425 (2011).
- ¹⁵K. M. M. Habib and R. K. Lake, *Phys. Rev. B* **86**, 045418 (2012).
- ¹⁶K. Wakabayashi and M. Sigrist, *Phys. Rev. Lett.* **84**, 3390 (2000).
- ¹⁷K. Wakabayashi, *Phys. Rev. B* **64**, 125428 (2001).
- ¹⁸H. Tong and M. W. Wu, *Phys. Rev. B* **85**, 205433 (2012).
- ¹⁹Z. Z. Zhang, K. Chang, and K. S. Chan, *Appl. Phys. Lett.* **93**, 062106 (2008).
- ²⁰Z. Z. Zhang, Z. H. Wu, K. Chang, and F. M. Peeters, *Nanotechnology* **20**, 415203 (2009).
- ²¹B. H. Zhou, W. H. Liao, B. L. Zhou, K.-Q. Chen, and G. H. Zhou, *Eur. Phys. J. B* **76**, 421 (2010).
- ²²B. Zhou, B. Zhou, A. Zeng, and G. Zhou, *Phys. Lett. A* **376**, 1710 (2012).
- ²³L. Rosales, P. Orellana, Z. Barticevic, and M. Pacheco, *Microelectron. J.* **39**, 537 (2008).
- ²⁴V. H. Nguyen, J. Saint-Martin, D. Querlioz, F. Mazzamuto, A. Bournel, Y.-M. Niquet, and P. Dollfus, *J. Comput. Electron.* **12**, 85 (2013).
- ²⁵S. B. Kumar, G. Seol, and J. Guo, *Appl. Phys. Lett.* **101**, 033503 (2012).
- ²⁶G. Fiori, A. Betti, S. Bruzzone, and G. Iannaccone, *ACS Nano* **6**, 2642 (2012).
- ²⁷L. Britnell, R. V. Gorbachev, R. Jalil, B. D. Belle, F. Schedin, A. Mishchenko, T. Georgiou, M. I. Katsnelson, L. Eaves, S. V. Morozov, N. M. R. Peres, J. Leist, A. K. Geim, K. S. Novoselov, and L. A. Ponomarenko, *Science* **335**, 947 (2012).
- ²⁸P. Zhao, R. Feenstra, G. Gu, and D. Jena, *IEEE Trans. Electron Devices* **60**, 951 (2013).
- ²⁹Y. Yoon and S. Salahuddin, *Appl. Phys. Lett.* **97**, 033102 (2010).
- ³⁰S. Khasanvis, K. M. M. Habib, M. Rahman, P. Narayanan, R. K. Lake, and C. A. Moritz, in *Proceedings of 2011 IEEE/ACM International Symposium on Nanoscale Architectures (NANOARCH)* (2011), pp. 189–195.
- ³¹S. Khasanvis, K. M. M. Habib, M. Rahman, P. Narayanan, R. K. Lake, and C. A. Moritz, in *Proceedings of 2012 IEEE/ACM International Symposium on Nanoscale Architectures (NANOARCH)* (2012), pp. 69–76.
- ³²K. M. M. Habib, A. Khitun, A. A. Balandin, and R. K. Lake, in *Proceedings of 2011 IEEE/ACM International Symposium on Nanoscale Architectures (NANOARCH)* (2011), pp. 86–90.
- ³³G. Kresse and J. Hafner, *Phys. Rev. B* **47**, 558 (1993).
- ³⁴S. B. Trickey, F. Müller-Plathe, G. H. F. Diercksen, and J. C. Boettger, *Phys. Rev. B* **45**, 4460 (1992).
- ³⁵Y.-W. Son, M. L. Cohen, and S. G. Louie, *Phys. Rev. Lett.* **97**, 216803 (2006).
- ³⁶H. Zheng, Z. F. Wang, T. Luo, Q. W. Shi, and J. Chen, *Phys. Rev. B* **75**, 165414 (2007).
- ³⁷D. Kienle, J. I. Cerda, and A. W. Ghosh, *J. Appl. Phys.* **100**, 043714 (2006).
- ³⁸C. Tang, W. Yan, Y. Zheng, G. Li, and L. Li, *Nanotechnology* **19**, 435401 (2008).
- ³⁹L. Brey and H. A. Fertig, *Phys. Rev. B* **73**, 235411 (2006).
- ⁴⁰J.-C. Charlier, X. Gonze, and J.-P. Michenaud, *Phys. Rev. B* **43**, 4579 (1991).
- ⁴¹L. Jiang, Y. Zheng, C. Yi, H. Li, and T. Lü, *Phys. Rev. B* **80**, 155454 (2009).